# Fluid-Structure Interaction of a Rolling Cylinder with Offset Centre-of-Mass

**Farah Yasmina Houdroge, Mark C. Thompson, Thomas Leweke and Kerry Hourigan**

**Abstract** With the aim of understanding discrepancies between experimental observations and numerical simulations for a cylinder rolling down an inclined plane, this study investigates the effect that offsetting the centre-of-mass from the cylinder centroid has on body forces, velocity and wake structures. The numerical cases considered focus on the same parameters as the referenced experiment: cylinder-to-fluid density ratio and wall inclination angle, for Reynolds numbers in a range around the critical value for the transition from stationary flow to periodic vortex shedding. The centre-of-mass is placed at a distance of up to 2 % of the diameter from the geometrical centre of the cylinder. It is found that the main features of the predicted wake flow are in good agreement with those observed experimentally. They include the inception of small-scale shear-layer vortices in the near wake, locked to the cylinder rotational frequency, as well as large-scale vortices further downstream. This is further confirmed through force and velocity histories, where two oscillations are found to operate at significantly different frequencies. While the amplitudes of the lift, drag and cylinder velocity oscillations see an increase with offset distance, the Strouhal numbers of the small- and large-scale structures remain unaffected and agree well with those measured in experiments at similar Reynolds numbers.

**Keywords** Bluff-body wake · Fluid-structure interaction · Rolling cylinder · Centre-of-mass offset

F.Y. Houdroge (✉) · M.C. Thompson · K. Hourigan
Department of Mechanical and Aerospace Engineering, Fluids Laboratory for Aeronautical and Industrial Research (FLAIR), Monash University, Melbourne, VIC 3800, Australia
e-mail: farah.houdroge@monash.edu

T. Leweke
IRPHE UMR 7342, CNRS, Aix-Marseille Université, Centrale Marseille, 13384 Marseille, France



M. Braza et al. (eds.), *Advances in Fluid-Structure Interaction*,
Notes on Numerical Fluid Mechanics and Multidisciplinary Design 133,
DOI 10.1007/978-3-319-27386-0_6

## 1 Introduction

The flow around a bluff body close to a boundary has relevance to a number of important physical applications. Many practical situations see bluff bodies near a wall and with rotation rates and trajectories predominantly determined by the drag and lift forces (as well as the torques). Some examples covering a wide Reynolds number range include biological flows such as cell-cell and cell-wall interactions, two-phase flows found in industrial processes (e.g., coal slurries) or natural environments (e.g., sediment transport), and sports such as Association Football (soccer), tennis, pétanque and golf that involve rotating balls translating and impacting on surfaces. Despite its seemingly generic nature, even the closely related problem of a cylinder rolling along a boundary under gravity has not yet been extensively researched, perhaps due to numerical modelling complications and difficulties in setting up controlled experiments. In fact, the majority of previous studies have focussed on cylinders and spheres placed in a free-stream, where wall interactions or induced rotation and vibration were neglected.

When body rotation is considered, studies by Tang and Ingham [1] showed that imposing a rotation on the cylinder renders the wake asymmetrical and, at low Reynolds number, the elimination of one or both of the recirculation regions in the wake is observed. This, of course, follows a long line of previous studies on rotating cylinders, with those of Magnus [2] and Prandtl [3] particularly notable. As the Reynolds numbers increases, imposed rotation may also suppress the onset of transition to unsteady flow (in comparison with a non-rotating body).

For bodies close to a wall, an early study by Taneda [4] showed that the presence of a stationary wall near a cylinder acts to stabilise the wake flow. In such cases, the steady flow is characterised by a single recirculation region that separates from the body and reattaches to the wall downstream, similar to the one observed for flow over a backward-facing step (Armaly et al. [5]). More recently, Stewart et al. [6] investigated the case of a rotating cylinder adjacent to a moving wall at various rotation rates. They found that prograde (normal) rolling destabilises the flow, whereas retrograde (reverse) rotation delays the onset of unsteady flow. When the flow becomes unsteady, the strength of the vortex shedding decreases as the cylinder is placed closer to the wall [7], and a vortex pair with a net non-zero circulation appears in the wake. It results from the interaction between the vortex formed from the shear layer shed from the top of the cylinder and secondary vorticity formation and lift-off from the wall shear layer downstream [6, 8], as illustrated in Fig. 1.

More recently, a two-dimensional numerical study was conducted on the flow characteristics and aerodynamic forces associated with a cylinder rolling freely along a solid inclined surface, i.e., with no constraints on either its velocity or rotation rate [9]. In this case, using a specific scaling, the final average state of the flow is determined by merely two governing parameters: the density ratio, $\beta$, defined as the ratio of the cylinder to the fluid density, and a Reynolds number, $\mathrm{Re}_f$, defined using a derived velocity scale representing the mean terminal velocity of the cylinder in both

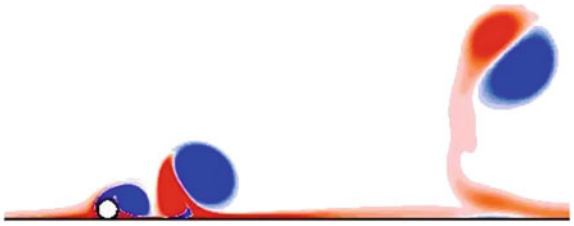

**Fig. 1** Vorticity contours in the wake of a cylinder (diameter $d$) rolling to the left at a constant fixed speed $U$ along a straight wall. The Reynolds number is $\mathrm{Re} = Ud/\nu = 200$ ($\nu$ kinematic viscosity). *Red* and *blue* represent positive and negative vorticity, respectively

the steady and unsteady cases. Subsequently, experiments in a water channel were conducted in an attempt to reproduce and validate some of these results, but the resulting wake flow structures and body motion were somewhat different from those observed numerically. This may be attributed to the challenging experimental setup that is required to match the idealized two-dimensional geometry and flow conditions of the numerical simulations. In fact, imperfections in experiments can lead to perturbations of the flow, which can significantly amplify and lead to substantially non-ideal behaviour. Similar effects have already been documented previously for other classes of flows, e.g. in [10–13].

For the current experiments, imperfections may include small burrs or eccentricity of the cylinder cross-section, bending in the spanwise direction, a non-planar wall, and an offset centre-of-mass. Here, the last effect is further considered numerically. It preserves the circular cross-section of the cylinder and represents a two-dimensional deviation, but it typifies a perturbation at the rolling frequency. One aim of this study is to determine the effect of such a perturbation on both the motion and wake of a low mass-ratio cylinder, and the sensitivity of the response to the level of the perturbation. Along the same lines, Mittal [14] carried out a numerical investigation of the flow past an eccentrically rotating cylinder in a free-stream. He found that the flow is unsteady, but that the mean values of the aerodynamic forces, as well as the flow structure, are similar to the case without eccentricity. The presence of the wall in the present study has a determining influence on the flow structure. We here seek to reproduce and investigate numerically the *wobbly* body motion and associated flow characteristics observed in the experiments. This study could then provide guidelines for future experiments and tolerance values for the manufacturing of components required for the study of rolling cylinder flow.

The outline of this paper is as follows. An overview of the problem under consideration is given in Sect. 2. Section 3 covers the methodology, numerical methods and experimental setup that were used. The computational and experimental results are presented, compared and discussed in Sect. 4. A summary and conclusion are given in Sect. 5.

## 2 Problem Definition

Figure 2 illustrates the problem under consideration, a circular cylinder rolling under gravity along a flat inclined surface, which is treated here in two dimensions. The different body forces exerted on the the cylinder are: the normal reaction $N$, lift $L$, drag $D$, the friction force $R$ and the weight $mg$. There is also a torque $(T)$ from viscous stresses at the cylinder surface. Other denoted entities are: the inclination angle $\theta$ of the wall, the velocity $U$ of the body, its radius $a$ and angular velocity $\omega$. For numerical simplicity, the origin of the frame of reference is fixed at the centre of the cylinder and moving with it along the wall.

The offset centre-of-mass position $(e)$ is defined by its distance $b$ to the geometric centre and by the initial offset angle $\varphi_0$ measured from the vertical, as shown on the left of Fig. 2. A non-dimensional offset parameter $r$ is given by the ratio of the offset distance to the radius of the cylinder: $r = b/a$ (expressed in %). $\rho_c$ and $\rho_f$ are the densities of the cylinder and of the fluid, respectively. The Reynolds number Re is based on the cylinder diameter and the asymptotic mean translation velocity of the cylinder: $\mathrm{Re} = 2a\overline{U}/\nu$.

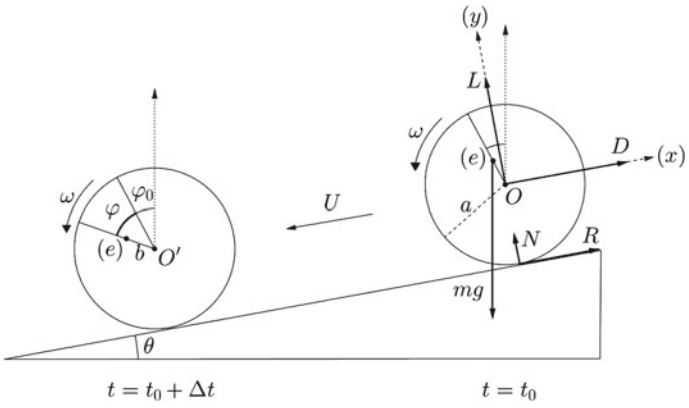


**Fig. 2** A schematic of the two-dimensional problem under consideration: on the *right*, at $t = t_0$, the cylinder of radius $a$ is rolling along an inclined plane of slope $\theta$, where $(e)$ represents its centre-of-mass. Its translational and angular velocities are $U$ and $\omega$, respectively. The frame-of-reference $(x,\ y)$ is attached to the centre of the body, and the different forces exerted on it are illustrated: the aerodynamic forces (drag $D$ and lift $L$), the mechanical forces (reaction of the wall on the body, $N$ and $R$) and gravity (weight $mg$). A viscous torque $T$ (not shown) also acts on the cylinder. On the *left*, the offset distance $b$ from the geometric centre is defined, as well as the initial offset angle $\varphi_0$ and the offset angle $\varphi$ after a time interval $\Delta t$

# 3 Methodology

## 3.1 Governing Equations

The governing equations are the two-dimensional continuity and Navier–Stokes equations for the motion of the fluid, and Newton's second law together with the angular momentum balance to describe the acceleration of the cylinder in terms of the forces acting on the centre-of-mass. In the case of an incompressible flow, the continuity equation is

$$\nabla \cdot \mathbf{u} = 0, \tag{1}$$

and the general form of the Navier–Stokes equation in an accelerating frame is

$$\frac{\partial \mathbf{u}}{\partial t} + \mathbf{u} \cdot \nabla \mathbf{u} = -\frac{1}{\rho_f} \nabla P + \nu \nabla^2 \mathbf{u} - \frac{\mathrm{d}\mathbf{U}}{\mathrm{d}t}. \tag{2}$$

$\mathbf{u} = (u,\ v)$ and $\mathbf{U} = (U,\ 0)$ are the fluid velocity and the translation velocity of the cylinder, respectively. The last term in the equation accounts for the acceleration of the moving frame-of-reference and is equal to the acceleration of the cylinder centroid. Using the notation defined in Fig. 2, the resulting equation of motion for the cylinder with an offset centre-of-mass is

$$\begin{aligned} m_c \left[a^2\ddot{\varphi} + 2ab\ddot{\varphi}\cos(\varphi + \varphi_0) + b^2\ddot{\varphi} - ab\dot{\varphi}^2 \sin(\varphi + \varphi_0)\right] + I_{cm}\ddot{\varphi} \\ = mga\sin\theta + mgb\sin(\varphi + \varphi_0 + \theta) - aD - T. \end{aligned} \tag{3}$$

Here, $m_c$ is the mass of the cylinder (per unit span), $m = (\rho_c - \rho_f)\pi a^2$ the apparent mass and $I_{cm} = I_0 - m_c b^2$ the moment of inertia at the centre-of-mass, with $I_0$ the moment of inertia about the geometric centre. In the following, it is assumed that $I_0 = \frac{1}{2}m_c a^2$, the moment of inertia for a uniform density disk. The drag force $D$, lift force $L$ and viscous torque $T$ can be expressed as

$$D = \frac{1}{2}(2a)\rho_f U^2 C_D = a\rho_f U^2 C_D, \tag{4}$$

$$L = \frac{1}{2}(2a)\rho_f U^2 C_L = a\rho_f U^2 C_L, \tag{5}$$

$$T = \frac{1}{2}(2a)a\rho_f U^2 C_T = a^2\rho_f U^2 C_T. \tag{6}$$

$C_D$, $C_L$ and $C_T$ are the drag, lift and viscous torque (or moment) coefficients, respectively. When the centre-of-mass coincides with the geometric centre of the cylinder ($b = 0$), Eq. (3) reduces to

$$\frac{\mathrm{d}U}{\mathrm{d}t} = \frac{2}{3}\left[\left(1 - \frac{1}{\beta}\right) g \sin\theta - \frac{D}{\pi a^2 \rho_c} - \frac{T}{\pi a^3 \rho_c}\right], \tag{7}$$

where $\beta = \rho_c / \rho_f$ is the density (or mass) ratio.

### 3.2 Non-dimensional Equations

Considering the case with no eccentricity, let $G = (\beta - 1)\, g \sin\theta$. When scaling lengths by the radius $a$, velocities by $V_f = \sqrt{aG}$ (which represents a qualitative estimate of the mean terminal velocity of the cylinder), time by $\tau = \sqrt{a/G}$ and pressure by $\rho_f V_f^2$, the non-dimensional forms (superscript *) of the continuity, Navier–Stokes and acceleration equations (Eqs. (1), (2) and (7), respectively) are

$$\nabla \cdot \mathbf{u}^* = 0, \tag{8}$$

$$\frac{\partial \mathbf{u}^*}{\partial t^*} + \mathbf{u}^* \cdot \nabla \mathbf{u}^* = -\nabla P^* + \frac{1}{\mathrm{Re}_f} \nabla^2 \mathbf{u}^* - \frac{\mathrm{d}\mathbf{U}^*}{\mathrm{d}t^*}, \tag{9}$$

$$\frac{\mathrm{d}U^*}{\mathrm{d}t^*} = \frac{2}{3\beta}\left[1 - \frac{U^{*2}}{\pi}\left(C_D + C_T\right)\right]. \tag{10}$$

$\mathrm{Re}_f = a V_f / \nu = a\sqrt{aG}/\nu$ is a newly defined Reynolds number and $U*$ the scaled (non-dimensional) velocity of the cylinder.

### 3.3 Numerical Formulation

The time-dependent incompressible Navier–Stokes equations for the fluid are solved in Cartesian coordinates using a spectral-element approach: the advection, pressure and diffusion terms are discretised using a second-order fractional time-stepping method [15, 16]. The spectral-element method is essentially a *P-based* high-order finite-element method that uses Lagrangian polynomial interpolants based on Gauss-Legendre-Lobatto integration points as internal nodes to form approximations to the governing partial-differential equations. It has the advantage of converging much faster than typical *H-based* finite-element methods, since the error decreases exponentially (or spectrally) with the order of the approximating polynomial, while retaining most of the flexibility of the finite elements to efficiently discretize the computational domain. The nodal-based approach adopted is given in [16]. The solver is explained in more detail in [17]. It has widely been tested, validated and used for studies of flows around bluff bodies such as cylinders [8, 18, 19] and spheres [17, 20, 21].

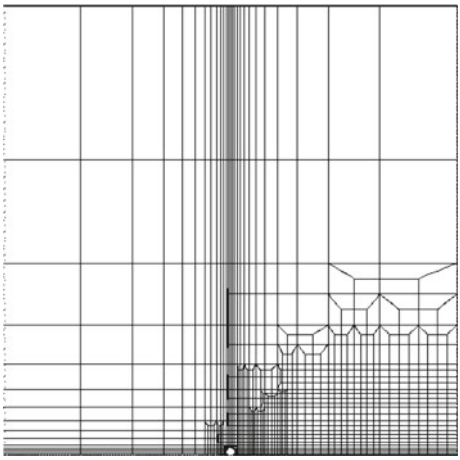

**Fig. 3** Schematic of the macro-element mesh. The cylinder is placed near the wall, with a small gap of $0.005d$ to avoid numerical singularities [6, 8, 22]. The flow is from *left* to *right*, and the resolution in the vicinity and downstream of the cylinder is increased, in order to accurately capture the flow structures in the wake

The mesh used for this study is shown in Fig. 3; it consists of 1552 nodes and 1472 elements. Typically, the results shown in this article used either $5 \times 5$ or $6 \times 6$ internal nodes per element. The dimensions of the computational domain are $L_x/d \times L_y/d = 50 \times 50$, where $d = 2a$ is the diameter of the cylinder. Thus the blockage ratio is 2 %. The body is located at the centre near the wall. Resolution studies were carried out on the domain size, number of nodes per element and chosen time step to ensure the convergence of the results. These studies indicate convergence of velocity, drag coefficient and Strouhal number to better than 1 % at the highest considered Reynolds number.

The following boundary conditions were applied for the numerical simulations. The cylinder rotates with no slip at the lower wall. At the top, bottom and inflow boundaries, the velocity is set to the negative of the cylinder's centroid velocity (in the absolute frame). At the right boundary, the normal velocity gradient conditions is applied and the pressure is set to zero. A higher-order pressure boundary condition is used at all solid surfaces [16] ensuring second-order accuracy of the velocity field.

## *3.4 Experimental Setup*

Experiments were carried out in a free-surface water tank of dimensions 150 cm (length) × 38 cm (width) × 50 cm (depth). A 2 cm thick Plexiglas plate was placed in the tank, which could be inclined with respect to the horizontal direction by using various sets of supports (see Fig. 4). The plate had a length of 130 cm and a width of 37.5 cm, extending between the two lateral walls of the tank. The cylinder used for the experiments reported here was a hollow Perspex tube of diameter $2a = 12$ mm and length 300 mm (aspect ratio 25), filled with water and sealed on both ends. Its (average) density was $\rho_c = 1.10$ g/cm$^3$, which at room temperature led to a density

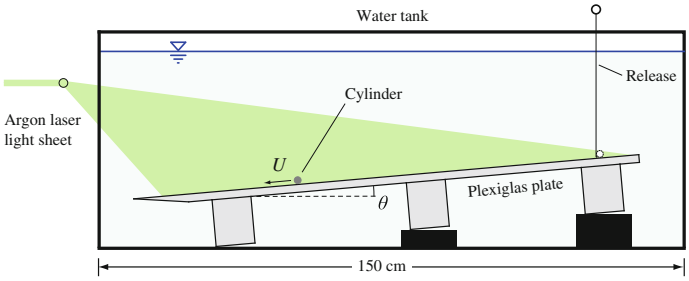


**Fig. 4** Schematic of the experimental setup

ratio $\beta = 1.10$. Prior to an experimental run, the cylinder was placed near the upper end of the plate and blocked by a thin metal wire. When the fluid motion in the tank had calmed down, the wire was removed and the cylinder was free to roll down the plate. For density ratios near 1, it reaches its terminal velocity very quickly, within less than 10 diameters from the start.

The wake structure of the freely rolling cylinder was visualised by laser-induced fluorescence [23]. Using a long metal cannula, an aqueous solution of fluorescein, slightly denser than the water in the tank, was deposited on the plate near the cylinder, where it spread along the surface. When the cylinder rolled across this dye layer, the dye was trapped in the vortical structures, thus visualising the wake. Illumination was achieved with a sheet of light from an argon ion laser, placed in the vertical plane of symmetry of the set-up in the centre of the tank. Video sequences of the visualised flow were recorded with a Nikon Coolpix P7800 digital camera, at a resolution of $1920 \times 1080$ pixels and a rate of 25 Hz. Quantitative information concerning the instantaneous and average cylinder velocities was obtained from these videos using the Open Source Physics *Tracker* software [24].

The results presented in the following section were obtained for a plate inclination angle $\theta = 1.9°$. The mean terminal velocity of the cylinder for this case was $\overline{U} = 1.35$ cm/s, leading to a Reynolds number $\mathrm{Re} = 160$ (the rescaled Reynolds number equals $\mathrm{Re}_f = 84$ for this configuration).

## 4 Results

### *4.1 Wake Structure*

In the computations, offsetting the centre-of-mass from the cylinder centroid results in a non-constant rolling velocity, varying over one rolling cycle. When the centre-of-mass is trailing the centroid and rising, the cylinder slows down. Conversely, when the centre-of-mass is preceding the centroid and falling, the cylinder accelerates. This forcing perturbation acts at the frequency of the rolling cycle and leads to periodic

vorticity concentrations forming in the upper separating shear-layer, which strongly resemble the structures observed experimentally.

Figure 5 shows the typical wake structures observed in experiments, and the one obtained by numerical simulation with a centre-of-mass offset of $r = 3.8\,\%$. The Reynolds number ($\mathrm{Re} = 160$) is above the critical value for the transition to unsteady flow ($\mathrm{Re}_c \simeq 89$ [9]), so there is periodic shedding of large-scale vortices into the wake, as is seen in both images. The numerical result on the right shows that the shear layer separating from the top of the cylinder feeds these large vortex structures in the near wake prior to their release into the far wake. However, the shear layer clearly also contains smaller-scale vortices triggered by the oscillatory component of the cylinder velocity. Thus the roll-up into larger-scale structures is complex. These smaller-scale shear layer vortices are also present in the experimental visualisation on the left of Fig. 5. There are a number of differences and possible deviations between the experimental and computational setups, including the fact that the experimental cylinder is not homogeneous in density, a non-uniformity in the cylinder geometry and/or the plate surface, an eccentricity of the cylinder surface, or three-dimensional and end effects. Some differences between the simulations and experiments should therefore be expected. However, importantly the oscillatory nature of the cylinder motion is observed in both cases and strongly affects the wake development.

A more detailed indication of the effect of a centre-of-mass offset on the near wake structure is shown in Fig. 6. This figure compares the wake vorticity distribution for the cases without perturbation and with an offset of $r = 3\,\%$ at $\mathrm{Re} = 115$. In the latter, the strong shear-layer vortices associated with the induced oscillating cylinder velocity are clearly seen, together with their influence on both the near and far wake structure.

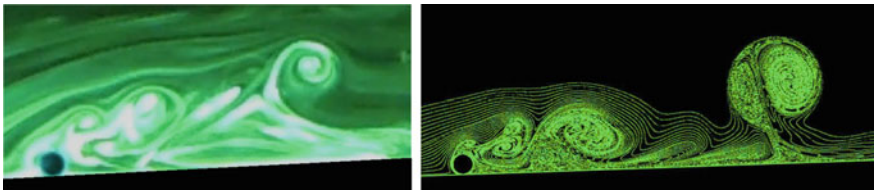

**Fig. 5** Typical wake flow structures from experiments and computations showing some of the main flow features of the wake. *Left* Experimental dye visualisation. *Right* Numerical simulations showing the wake visualised by passive tracer particles released from upstream and near the rear of the cylinder. In both cases, $\mathrm{Re} = 160$, $\theta = 1.9°$ and $\beta = 1.10$. For the numerical simulation $r = 3.8\,\%$

**Fig. 6** Coloured vorticity contour showing the effect of an offset centre-of-mass on the wake flow. *Left* Unperturbed flow. *Right* Perturbed flow for $r = 3\,\%$. $\mathrm{Re} = 115$, $\beta = 1.10$ and $\theta = 1.9°$

**Fig. 7** Numerical flow visualisation of the shear-layer vortices in the wake of the cylinder at Re = 88, $\theta = 1.9°$, $\beta = 1.10$ and $r = 2\,\%$. The image on the *left* shows vorticity contours and the one on the *right* shows a visualisation of the wake using passive tracer particles released near the rear surface of the cylinder

Figure 7 shows the flow structure predicted from numerical simulation for Re = 88, just below the transition to two-dimensional vortex shedding [6, 9], and $r = 2\,\%$. As before, the shear-layer vortices dominate the separating shear layer and again match well with the experimental visualisations of the near wake at the higher Reynolds number shown previously. However, there is no large-scale shedding of vortices in this case. The smaller-scale shear layer vortices sufficiently cross-diffuse as they advect downstream so that large-scale shedding does not occur.

As indicated above, for the simulations reported here, the inclination angle of the wall and the density ratio are set to $\theta = 1.9°$ and $\beta = 1.10$, respectively, corresponding to the experimental case at Re = 160. Interestingly, at this low slope angle, Eq. 3 is in its most downstream position, the loss of gravitational energy as the cylinder moves down the slope is exactly balanced by the gain in potential energy due to lifting the cylinder centre-of-mass vertically, when the offset has the particular value $r = \sin\theta = 0.033$. For significantly larger offset values, the cylinder may stop, or not even start, rolling. In the numerical simulations, this situation was observed for $r = 0.04$, i.e., for an offset of just 2 % of the diameter, when the initial offset angle was $\varphi_0 = -90°$.

## *4.2 Body Forces and Velocity*

A more detailed numerical exploration of the centre-of-mass offset was carried out for two different Reynolds numbers, Re = 88 and Re = 130, including 11 offset values ranging from $r = 0$ (no offset) to $r = 2\,\%$. As the centre-of-mass is placed further away from the geometric centre, the time-mean values of the velocity, drag force and lift force increase in comparison with the no-offset case. At the maximum offset distance tested here ($r = 2\,\%$), an increase of the order of 10 % was obtained for the lift force, which is significantly higher than the 2 % increase in the velocity and drag force.

Time histories of the drag and lift coefficients, and of the non-dimensional cylinder velocity, are shown in Fig. 8 for Re = 88 and in Fig. 9 for Re = 130, for three offset values ($r = 0$, 1 and 2 %). Velocity and time are scaled as specified in Sect. 3.2. These plots, along with Fig. 10, show that the amplitude of the velocity oscillations increases almost linearly with the offset distance. The velocity and lift coefficient variations

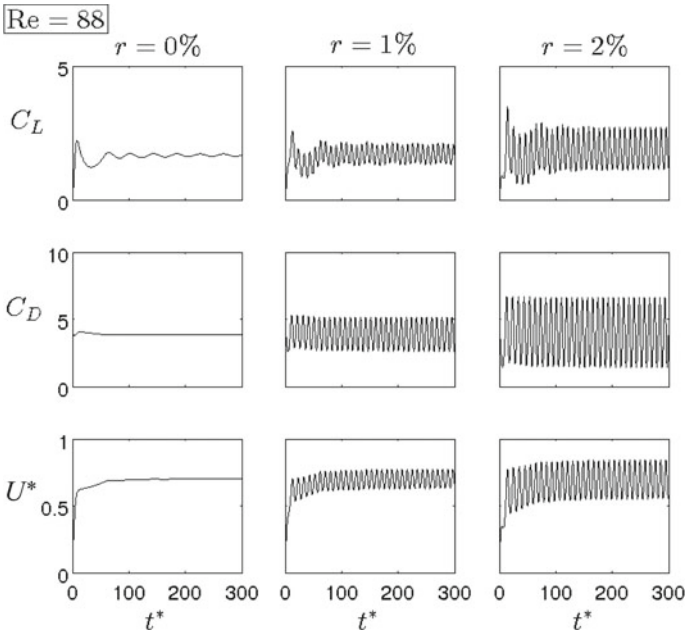


**Fig. 8** Lift and drag coefficients and cylinder velocity as function of time, at Re = 88 and $r = 0\,\%$ (*first column*), $r = 1\,\%$ (*second column*) and $r = 2\,\%$ (*third column*)

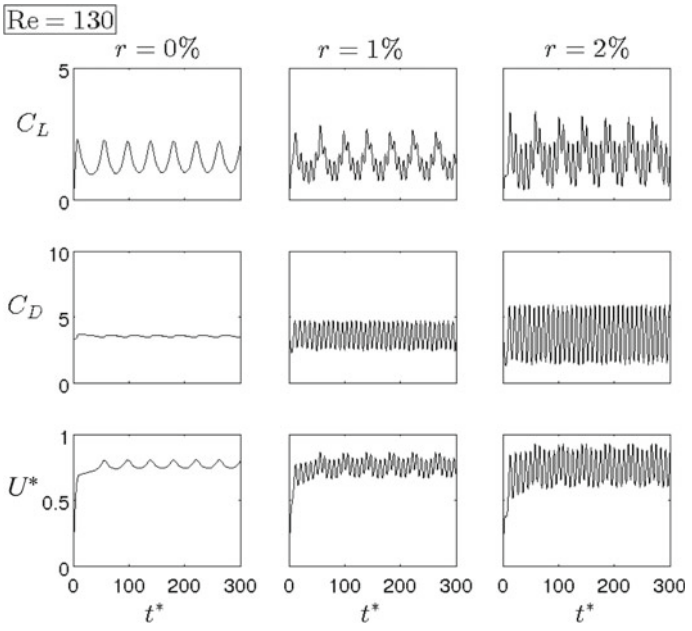


**Fig. 9** Lift and drag coefficients and cylinder velocity as function of time, at Re = 130 and $r = 0\,\%$ (*first column*), $r = 1\,\%$ (*second column*) and $r = 2\,\%$ (*third column*)

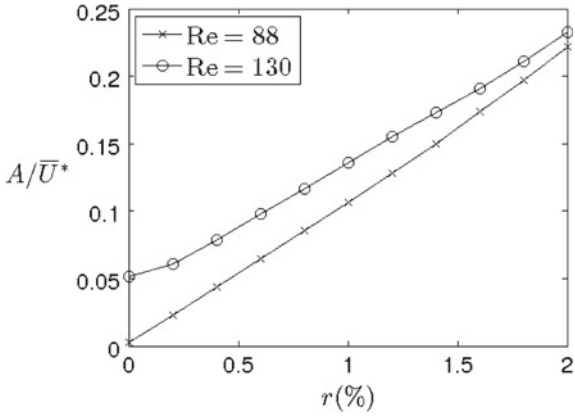


**Fig. 10** Plot of the mean velocity amplitude versus the offset ratio at Re = 88 and Re = 130. The amplitude is scaled by the mean terminal velocity of the cylinder

at the higher Reynolds number (Fig. 9) conform with the observations of the flow structure in the experiments: the rolling cylinder exhibits a wobble that perturbs the flow as it rolls down the slope. As a result, two superimposed oscillations can be observed that have significantly different periods, associated with the small-scale shear-layer vortices and the large-scale shedding. Furthermore, the Strouhal numbers calculated for these flows were found to be constant for all offset values ($r > 0$) tested here, and they are in good agreement with the ones found in the experiment of Sect. 4.1. These Strouhal numbers can be determined from the relations $St^{(1)} = 2a/\lambda$ and $St^{(2)} = 2af/\overline{U}$, where $\lambda$ is the streamwise separation distance between large-scale vortices and $f$ the shedding frequency of the smaller shear-layer vortices. Numerically one obtains $St^{(1)}_{num} = 0.0603$ and $St^{(2)}_{num} = 0.315$, versus $St^{(1)}_{exp} = 0.067$ and $St^{(2)}_{exp} = 0.32$ found experimentally. The higher Strouhal number is essentially the rolling frequency of the cylinder (given by $St = 1/\pi$), i.e., the period of the perturbation is imposed by the offset centre-of-mass.

## 5 Conclusions

The present investigation was motivated by an observed qualitative discrepancy between earlier numerical predictions of the flow around cylinders rolling freely down an inclined flat surface and recent experimental observations concerning the same geometry. Among the numerous possible imperfections that may affect the structure of the flow in the experiment, the focus here is on an offset of the centre-of-mass of the cylinder, allowing investigation within a two-dimensional framework. One consequence of increasing the offset distance is that the amplitude of the cylinder velocity oscillations grows, causing the development of increasingly large shear-layer vortices. The main characteristics of the wake predicted numerically are in good agreement with those observed in experiment, showing vortex formation in the top

separating shear layer at the cylinder rotational frequency. This adds considerably to the complexity of the formation of large-scale vortices in the near wake, which in turn are shed downstream at a frequency that is approximately one fifth of the shear-layer frequency. The two predicted Strouhal numbers are in good agreement with those measured experimentally. Although the match between experiment and simulation is not perfect, the present results highlight the strong effect that seemingly small perturbations can have on the overall large-scale flow around the freely rolling cylinder, and they underline the difficulties and the special care that is required when comparing and interpreting experimental and numerical results for certain sensitive flow configurations.

**Acknowledgments** The support from Australian Research Council Discovery Grants DP130100822, DP150102879 and computing time from the National Computational Infrastructure (NCI) and Pawsey Supercomputing Centre are gratefully acknowledged.

## References

1. Tang, T., Ingham, D.B.: On steady flow past a rotating circular cylinder at Reynolds numbers 60 and 100. Comput. Fluids **19**, 217–230 (1991)
2. Magnus, G.: Ueber die Abweichung der Geschosse, und: Ueber eine auffallende Erscheinung bei rotirenden Körpern. Annalen der Physik **164**, 1–29 (1853)
3. Prandtl, L.: Application of the "Magnus effect" to the wind propulsion of ships. Technical Report NACA-TM-367, National Advisory Committee for Aeronautics, Washington, DC (1926)
4. Taneda, S.: Experimental investigation of vortex streets. J. Phys. Soc. Jpn. **20**, 1714 (1965)
5. Armaly, B.F., Durst, F., Pereira, J.C.F., Schönung, B.: Experimental and theoretical investigation of backward-facing step flow. J. Fluid Mech. **127**, 473–496 (1983)
6. Stewart, B.E., Thompson, M.C., Leweke, T., Hourigan, K.: The wake behind a cylinder rolling on a wall at varying rotation rates. J. Fluid Mech. **648**, 225–256 (2010)
7. Lei, C., Cheng, L., Kavanagh, K.: Re-examination of the effect of a plane boundary on force and vortex shedding of a circular cylinder. J. Wind Eng. Ind. Aerodyn. **80**, 263–286 (1999)
8. Rao, A., Stewart, B.E., Thompson, M.C., Leweke, T., Hourigan, K.: Flows past rotating cylinders next to a wall. J. Fluids Struct. **27**, 668–679 (2011)
9. Houdroge, F.Y., Hourigan, K., Leweke, T., Thompson, M.C.: Fluid-structure interaction of a cylinder rolling down an incline under gravity. In: Proceedings of the 19th Australasian Fluid Mechanics Conference. Paper 459, AFMS, Melbourne, 2014
10. Thompson, M.C., Hourigan, K.: The sensitivity of steady vortex breakdown bubbles in confined cylinder flows to rotating lid misalignment. J. Fluid Mech. **496**, 129–138 (2003)
11. Brøns, M., Thompson, M.C., Hourigan, K.: Dye visualization near a three-dimensional stagnation point: application to the vortex breakdown bubble. J. Fluid Mech. **622**, 177–194 (2009)
12. Brøns, M., Shen, W.Z., Sørensen, J.N., Zhu, W.J.: The influence of imperfections on the flow structure of steady vortex breakdown bubbles. J. Fluid Mech. **578**, 453–466 (2007)
13. Lucor, D., Xiu, D., Su, C.H., Karniadakis, G.E.: Predictability and uncertainty in CFD. Int. J. Numer. Methods Fluids **43**, 483–505 (2003)
14. Mittal, S.: Flow past rotating cylinders: effect of eccentricity. J. Appl. Mech. **68**, 543–552 (2000)
15. Chorin, A.J.: Numerical solution of the Navier-Stokes equations. Mathematics of Computation, pp. 745–762 (1968)

16. Karniadakis, G.E., Israeli, M., Orszag, S.A.: High-order splitting methods for the incompressible Navier-Stokes equations. J. Comput. Phys. **97**, 414–443 (1991)
17. Thompson, M.C., Hourigan, K., Cheung, A., Leweke, T.: Hydrodynamics of a particle impact on a wall. Appl. Math. Model. **30**, 1356–1369 (2006)
18. Thompson, M.C., Leweke, T., Williamson, C.H.K.: The physical mechanism of transition in bluff body wakes. J. Fluids Struct. **15**, 607–616 (2001)
19. Ryan, K., Thompson, M.C., Hourigan, K.: Three-dimensional transition in the wake of bluff elongated cylinders. J. Fluid Mech. **538**, 1–29 (2005)
20. Thompson, M.C., Leweke, T., Provansal, M.: Kinematics and dynamics of sphere wake transition. J. Fluids Struct. **15**, 575–586 (2001)
21. Rao, A., Passaggia, P.Y., Bolnot, H., Thompson, M.C., Leweke, T., Hourigan, K.: Transition to chaos in the wake of a rolling sphere. J. Fluid Mech. **695**, 135–148 (2012)
22. Stewart, B.E., Hourigan, K., Thompson, M.C., Leweke, T.: Flow dynamics and forces associated with a cylinder rolling along a wall. Phys. Fluids **18**, 111701 (2006)
23. Leweke, T.: Dye visualization—a method for investigating biomechanical flows. Curr. Pharm. Biotechnol. **13**, 2141–2152 (2012)
24. Brown, D.: Tracker—video analysis and modeling tool. http://physlets.org/tracker/. Accessed 9 Sept 2015